Available online at www.sciencedirect.com
ScienceDirect
Engineering Structures 29 (2007) 88–100
ENGINEERING STRUCTURES
www.elsevier.com/locate/engstruct

Behavior of suspended roofs under blast loading

Ioannis G. Raftoyiannis*, Constantine C. Spyrakos, George T. Michaltsos

Department of Civil Engineering, National Technical University of Athens, 9 Iroon Polytechneiou Street, Zografou Campus, Athens 15780, Greece

Received 5 January 2006; received in revised form 31 March 2006; accepted 18 April 2006
Available online 8 June 2006

Abstract

This work deals with the nonlinear dynamic behavior of initially imperfect dissipative multi-suspended roof systems under blast loading. For various realistic combinations of geometrical, stiffness and damping parameters, the systems do not experience either snapping or large amplitude chaotic motions, contrary to findings reported for single and double suspension roof systems. A nonlinear analysis is employed to establish that global stability, being the main feature of multiple suspension roof systems, is captured by the proposed autonomous conservative models. Applying Lagrange's equations, the corresponding set of equations of motion for discrete models of multiple suspension roofs is obtained. Then, numerical integration of the equations of motion is performed via the Runge–Kutta scheme. The dynamic behavior of suspended roofs under blast loading is thoroughly examined for two cases of internal and external blast: source near the supports and source away from the supports. The problem is formulated in a simple manner that can be easily employed for preliminary design of multi-suspended roofs subjected to blast loads.

Keywords: Blast loads; Nonlinear dynamic analysis; Multi-suspended roofs

1. Introduction

Suspended roof systems are extensively used in many structural applications, such as commercial halls, airport halls, sport centers, trade and exhibition centers. Such structural systems combine aesthetics and economy to satisfy special architectural demands. Inspired engineers, such as L. Mies van der Rohe, K. Tange, P. L. Nervi, and others, have designed and built numerous great buildings with suspended roofs as their main structural component [1–4]. The Crown Hall at the Illinois Institute of Technology (1950–56), the Tokyo Small Olympics Arena (early 1960s), Dulles International Airport (Washington DC, 1962), the Stadthalle (Bremen 1964), the Europahalle (Karlsruhe 1983), the PA Tech Laboratories (Princeton 1986), the Church of Fatima (Brasilia 1988) and the Salt Lake City site for the XIX Olympic Winter Games of 2002 are representative examples of inspired applications of suspension roof systems.

In the last two decades, the development of powerful computers and sophisticated nonlinear FEM software has enabled engineers to utilize suspension roofs for complex large-scale structures classified among unique examples of engineering excellence. Suspended roof systems require three-dimensional suspensions and transverse stiffening, being sensitive to horizontal vibrations and may lose their stability caused by dynamic snap-through buckling [5–8]. Nevertheless, double and multiple suspension roofs may overcome disadvantages of single suspensions with repeated plane configurations, that can effectively resist uplift and unbalanced as well as upward and downward loading, as illustrated schematically in Fig. 1. A characteristic example of the double suspension roofing technique is the

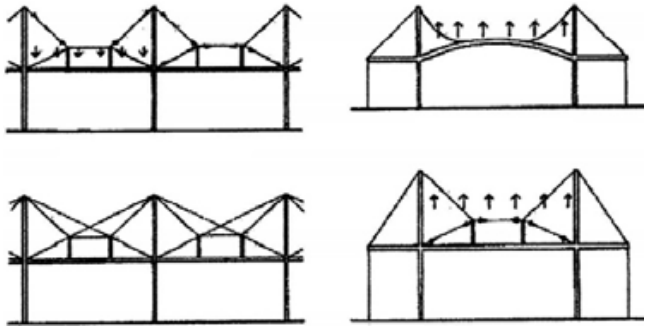

Fig. 1. Double suspension roof models.

* Corresponding author. Tel.: +30 2107 722454; fax: +30 2107 722482.
E-mail addresses: rafto@central.ntua.gr (I.G. Raftoyiannis), spyrakos@hol.gr (C.C. Spyrakos), michalts@central.ntua.gr (G.T. Michaltsos).

0141-0296/$ - see front matter © 2006 Elsevier Ltd. All rights reserved.
doi:10.1016/j.engstruct.2006.04.006

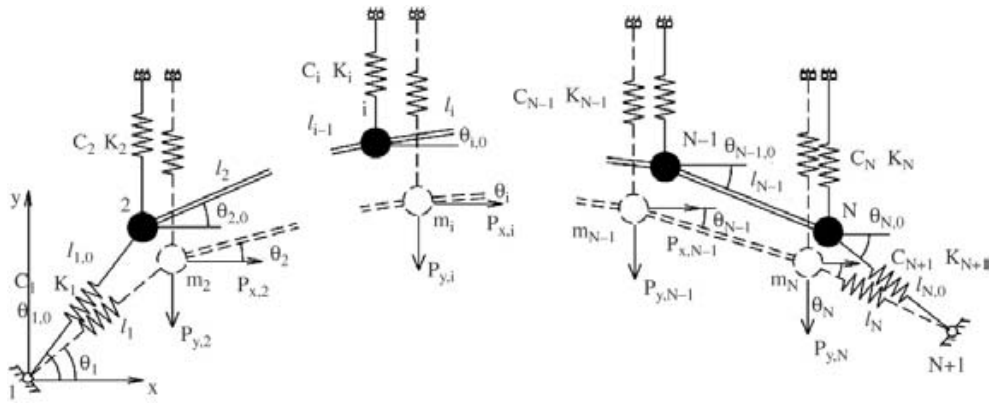

Fig. 2. N-DOF system simulating a multiple suspension roof.

one applied for the Bangkok International Trade and Exhibition Center (BITEC) [4].

Current state-of-practice for nonlinear static and dynamic analysis of suspended structures, including suspension roof systems, employs sophisticated FEM programs that simulate the actual structures with multiple degree-of-freedom (DOF) models [9,10]. Modeling of suspension roof systems with finite elements for design purposes is a time consuming procedure that requires special experience on stability matters. However, simple models of suspension roof systems with a few degrees-of-freedom can be used in order to capture the most pronounced dynamic behavior aspects of real continuous structures, provided that the simple models account for the salient features of the structural system [5]. Earlier and recent studies [11,12] have investigated the dynamic behavior and stability of simple 2-DOF and 3-DOF initially imperfect models with damping under step-loading that simulate single and double suspension roofs [13,14]. Important findings have been reported regarding sensitivity to horizontal vibrations, and limit point with different types of point attractor response as well as mathematical difficulties arising from the duration of motion before the transient response is damped out.

The present work deals with the nonlinear dynamic analysis of a multi-DOF initially imperfect dissipative model under internal and external blast loading, a type of loading for which, according to the authors' knowledge, there is increased interest but very limited information in the literature [15–17]. The formulation can consider inelastic behavior; however, this work examines the response of linear elastic systems accounting only for geometric nonlinearity. Based on energy principles, it is found that the dominant degrees-of-freedom, i.e., the vertical displacements, exhibit monotonically rising equilibrium paths implying global stability, regardless of the values of the parameters involved [13,14]. In this manner, this major advantage of multiple suspension roofs is verified and the corresponding dynamic response is proven to be stable. It should be noted that some modern suspension roof systems consist of thin shells suspended by cables [12,18]. Thus, the behavior of this type of structure may be quite different from the one predicted by the proposed model.

2. Model description and equations of motion

The majority of suspension roof structures consist of a space truss system with hinges, a number of suspension bars holding the system at the connection places, and are founded on elastic supports. The N-DOF dissipative system shown in Fig. 2 is used in this study as a simple, yet realistic, simulation of multi-suspension roofs [14]. The model consists of $N-1$ vertical linear springs with stiffness k_i $(i = 2, 3, \ldots, N)$ and corresponding dashpots c_i $(i = 2, 3, \ldots, N)$, while the $N-1$ concentrated masses m_i $(i = 2, 3, \ldots, N)$ are interconnected via $N-2$ weightless rigid inextensional bars with length ℓ_i. The nodal supports 1 and $N+1$ are immovable hinges connected with the masses m_2 and m_N through inclined springs with stiffness k_1 and k_{N+1}, and dashpots c_1 and c_{N+1}, respectively. Since the suspension springs 2 to N are acting mainly in the vertical direction and the system is anticipated to experience reasonably small horizontal deflections compared to its dimension, it can be assumed that the supports of the vertical springs can freely slide along horizontal tracks as shown in Fig. 2. The elastic supports are modeled with the springs k_1 and k_{N+1} considered as extensional bars with initial length $\ell_{1,0}$ and $\ell_{N,0}$, respectively, while in the deformed state their length becomes ℓ_1 and ℓ_N, respectively. Thus, the initial configuration of the system can be fully described by the bar lengths $\ell_{1,0}, \ell_2, \ldots, \ell_{N-1}$ and $\ell_{N,0}$, and the corresponding angles of direction $\theta_{1,0}, \theta_{2,0}, \ldots, \theta_{N-1,0}$ and $\theta_{N,0}$. Since nodes 1 and $N+1$ are immovable hinges, the deformed configuration is fully described by the bar length ℓ_1 and the angles $\theta_1, \theta_2, \ldots, \theta_{N-1}$.

The system is initially at rest in a configuration described as follows:

$$\left.\begin{aligned} x_{i,0} &= \ell_{1,0}\cos\theta_{1,0} + \sum_{j=2}^{i} \ell_j \cos\theta_{j,0} \\ y_{i,0} &= \ell_{1,0}\sin\theta_{1,0} + \sum_{j=2}^{i} \ell_j \sin\theta_{j,0} \end{aligned}\right\} \tag{1}$$

where $x_{i,0}$ and $y_{i,0}$ are the initial coordinates of joint i, and ℓ_j and $\theta_{j,0}$ are the length and the initial direction of bar j, respectively.

The deformed configuration of the system is described by

$$\left.\begin{aligned} x_i &= \ell_1 \cos\theta_1 + \sum_{j=2}^{i} \ell_j \cos\theta_j \\ y_i &= \ell_1 \sin\theta_1 + \sum_{j=2}^{i} \ell_j \sin\theta_j \end{aligned}\right\} \tag{2}$$

where x_i and y_i are the coordinates of joint i, and θ_j is the direction of bar j in the deformed position. The strain energy U of the system can be expressed as

$$\begin{aligned} U = {} & \frac{1}{2}k_1(\ell_1 - \ell_{1,0})^2 + \frac{1}{2}\sum_{i=2}^{N} k_i \left(\ell_1 \sin\theta_1 + \sum_{j=2}^{i-1} \ell_j \sin\theta_j \right. \\ & \left. - \ell_{1,0}\sin\theta_{1,0} - \sum_{j=2}^{i-1} \ell_j \sin\theta_{j,0} \right)^2 \\ & + \frac{1}{2}k_{N+1} \left\{ \left[\left(\ell_{1,0}\cos\theta_{1,0} + \sum_{j=2}^{N-1} \ell_j \cos\theta_{j,0} \right. \right. \right. \\ & \left. + \ell_{N,0}\cos\theta_{N,0} - \sum_{j=1}^{N-1} \ell_j \cos\theta_j \right)^2 \\ & + \left(\ell_{1,0}\sin\theta_{1,0} + \sum_{j=2}^{N-1} \ell_j \sin\theta_{j,0} + \ell_{N,0}\sin\theta_{N,0} \right. \\ & \left. \left. \left. - \sum_{j=1}^{N-1} \ell_j \sin\theta_j \right)^2 \right]^{\frac{1}{2}} - \ell_{N,0} \right\}. \end{aligned} \tag{3}$$

Since the system is modeled with concentrated masses m_i and the rotational inertia of the rigid links is ignored, the load potential Ω due to the blast loads $P_i(t)$ is given by

$$\begin{aligned} \Omega = {} & -\sum_{i=2}^{N} P_{x,i}(t) \left[\ell_1 \cos\theta_1 + \sum_{j=2}^{i-1} \ell_j \cos\theta_j - \ell_{1,0}\cos\theta_{1,0} \right. \\ & \left. - \sum_{j=2}^{i-1} \ell_j \cos\theta_{j,0} \right] - \sum_{i=2}^{N} P_{y,i}(t) \left[\ell_1 \sin\theta_1 \right. \\ & \left. + \sum_{j=2}^{i-1} \ell_j \sin\theta_j - \ell_{1,0}\sin\theta_{1,0} - \sum_{j=2}^{i-1} \ell_j \sin\theta_{j,0} \right]. \end{aligned} \tag{4}$$

The kinetic energy K of the system is

$$\begin{aligned} K = {} & \frac{1}{2}\sum_{i=2}^{N} m_i \left[\left(\dot{\ell}_1 \cos\theta_1 - \ell_1\dot{\theta}_1 \sin\theta_1 - \sum_{j=2}^{i-1} \ell_j\dot{\theta}_j \sin\theta_j \right)^2 \right. \\ & \left. + \left(\dot{\ell}_1 \sin\theta_1 + \ell_1\dot{\theta}_1 \cos\theta_1 + \sum_{j=2}^{i-1} \ell_j\dot{\theta}_j \cos\theta_j \right)^2 \right] \end{aligned} \tag{5}$$

and the dissipation energy F is given by

$$\begin{aligned} F = {} & \frac{1}{2}c_1(\dot{\ell}_1^2 + \ell_1^2\dot{\theta}_1^2) \\ & + \frac{1}{2}\sum_{i=2}^{N} c_i \left(\dot{\ell}_1 \sin\theta_1 + \sum_{j=1}^{i-1} \ell_j\dot{\theta}_j \cos\theta_j \right)^2 \\ & + \frac{1}{2}c_{N+1} \left[\left(\dot{\ell}_1 \cos\theta_1 - \sum_{j=1}^{N-1} \ell_j\dot{\theta}_j \sin\theta_j \right)^2 \right. \\ & \left. + \left(\dot{\ell}_1 \sin\theta_1 + \sum_{j=1}^{N-1} \ell_j\dot{\theta}_j \cos\theta_j \right)^2 \right]. \end{aligned} \tag{6}$$

The Lagrange equations of motion of the system are expressed by

$$\left.\begin{aligned} & \frac{\partial}{\partial t}\left(\frac{\partial K}{\partial \dot{\ell}_1}\right) - \frac{\partial K}{\partial \ell_1} + \frac{\partial F}{\partial \dot{\ell}_1} + \frac{\partial U}{\partial \ell_1} = -\frac{\partial \Omega}{\partial \ell_1} \\ & \frac{\partial}{\partial t}\left(\frac{\partial K}{\partial \dot{\theta}_1}\right) - \frac{\partial K}{\partial \theta_1} + \frac{\partial F}{\partial \dot{\theta}_1} + \frac{\partial U}{\partial \theta_1} = -\frac{\partial \Omega}{\partial \theta_1} \\ & \cdots \\ & \frac{\partial}{\partial t}\left(\frac{\partial K}{\partial \dot{\theta}_{N-1}}\right) - \frac{\partial K}{\partial \theta_{N-1}} + \frac{\partial F}{\partial \dot{\theta}_{N-1}} + \frac{\partial U}{\partial \theta_{N-1}} = -\frac{\partial \Omega}{\partial \theta_{N-1}} \end{aligned}\right\}. \tag{7}$$

The system depicted in Fig. 2 is considered initially imperfect, which implies that some joints have already undergone a small initial deformation for which all springs are considered to be unstressed. The blast forces $P_i(t)$ $(i = 2, \ldots, N)$ are applied at the joints in the form of horizontal and vertical components, i.e. $P_{x,i}(t)$ and $P_{y,i}(t)$.

According to previous research findings on internal blast loading [16], a simplified analysis can be performed by approximating the internal pressure–time loading function assuming that the pulses have the triangular shape shown in Fig. 3 for both incident (the largest triangle) and reflected waves, in which time t_a denotes the arrival time and T_r the equivalent positive phase duration of the reflected wave. According to Baker et al. [15], the peak pressure p_r is halved on each re-reflection, while after three reflections the pressure of any reflected wave can be assumed to be practically zero. The main parameters involved in the pressure function are: the pressure p_r, the arrival time t_a and the positive phase duration T_r. The internal pressure loading function $P(t)$ for internal blast with respect to time t can be expressed by [15]:

$$\left.\begin{aligned} & \frac{t_a + T_r - t}{T_r} p_r && t_a < t < t_a + T_r \\ & \frac{3t_a + T_r - t}{2T_r} p_r && 3t_a < t < 3t_a + T_r \\ & \frac{5t_a + T_r - t}{4T_r} p_r && 5t_a < t < 5t_a + T_r \\ & 0 && \text{elsewhere} \end{aligned}\right\}. \tag{8}$$

A typical pressure–time profile for an external blast wave is shown in Fig. 4, in which the effect of underpressure is also included. It consists of a straight line up to the raise time t_1 followed by an exponential decay through the positive phase (up to time $t_1 + t_2$) into the negative phase ($t > t_1 + t_2$), finally becoming asymptotic to the time axis. The parameters

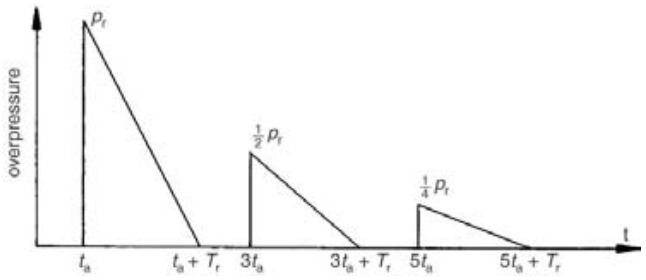

Fig. 3. Internal blast loading function.

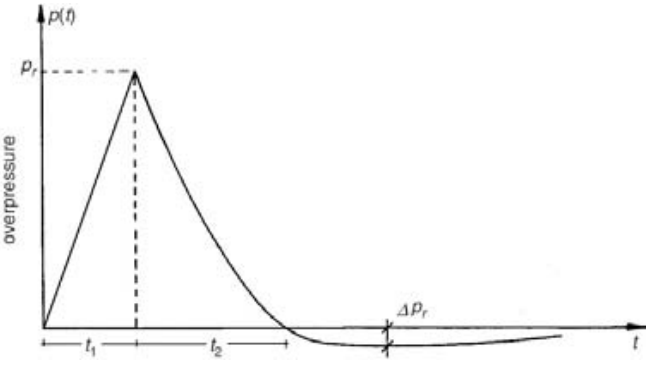

Fig. 4. External blast loading function.

involved in the pressure function are: the pressure p_r, the raise time t_1, the positive phase duration t_1+t_2 and the underpressure component Δp_r related to the exponential factor a as expressed in Eq. (9). For external blast the pressure loading function $P(t)$ is expressed as follows [16]:

$$\left.\begin{array}{ll} p_r \dfrac{t}{t_1} & 0 < t < t_1 \\ p_r \left[1 - \dfrac{t - t_1}{t_2 - t_1}\right] \mathrm{e}^{-a(t-t_1)} & t > t_1 \end{array}\right\}. \tag{9}$$

The following nondimensional quantities are introduced into Eqs. (7):

$$\left.\begin{array}{l} \lambda = \dfrac{P_2}{k_1 \ell_{1,0}}, \tau = \sqrt{\dfrac{k_1}{m_2}}\, t, \overline{\ell}_{N,0} = \ell_{N,0}/\ell_{1,0} \\ \overline{m}_i = m_i/m_2,\ p_i = P_i/P_2, \overline{\ell}_i = \ell_i/\ell_{1,0}\ (i = 2, \ldots, N) \\ \overline{c}_i = c_i/\sqrt{k_1 m_2}, \overline{k}_i = k_i/k_1, \overline{x}_i = x_i/\ell_{1,0}, \overline{y}_i = y_i/\ell_{1,0} \end{array}\right\} \tag{10}$$

where k_1 and $\ell_{1,0}$ are the stiffness and the initial length of the left support spring, respectively, and m_2 and P_2 are the mass and total magnitude of impact force at node 2, respectively. After manipulation of the resulting expressions for each model case (i.e. for various values of N), the equations of motion can be formulated and solved in a nondimensional form. Appendix presents the nondimensional equations of motion for the 3-DOF system without damping. Numerical difficulties caused by strong nonlinearities associated with convergence failure have been faced in the process of solving Eqs. (7). This problem has been efficiently treated by decreasing the size of the relevant integration step, with negligible effect on the accuracy of the results, as elaborated in the following section.

3. Numerical results and discussion

The numerical examples presented herein refer to the doubly and triply suspended roof models with the 3-DOF and 4-DOF systems shown in Fig. 5. For a wide range of representative geometrical configurations and combinations of material properties, the dynamic response of each system is obtained considering global stability for various internal and external blast loads applied to shallow roof configurations.

3.1. Double suspension roof model

The corresponding 3-DOF model with $\overline{\ell}_2 = 6, \overline{\ell}_{3,0} = 1, \overline{m}_3 = 1$ and $\theta_{1,0} = -\theta_{3,0} = 45°$ is shown in Fig. 5(a). The suspension stiffness ($k_2 = k_3$) has been varied with reference to the lateral support stiffness ($k_1 = k_4$) and the following cases have been studied: (i) strong suspension system ($\overline{k}_2 = \overline{k}_3 = 1$), (ii) medium stiffness suspension system ($\overline{k}_2 = \overline{k}_3 = 0.5$), and (iii) low stiffness suspension system ($\overline{k}_2 = \overline{k}_3 = 0.1$). In all

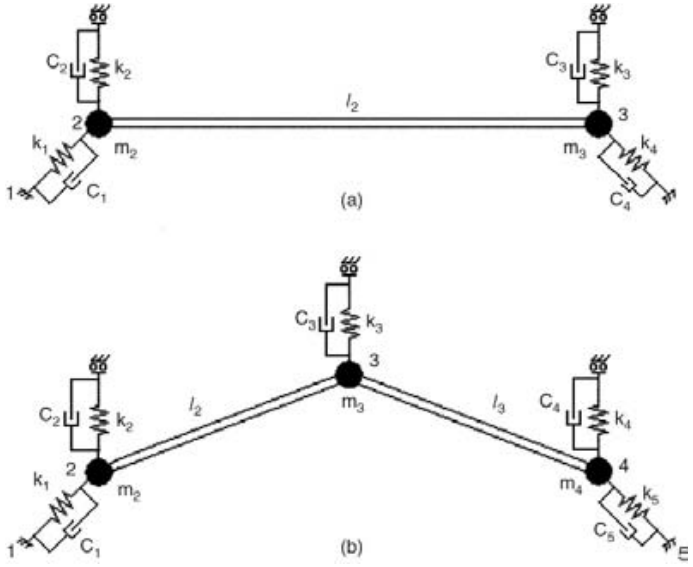

Fig. 5. 3-DOF and 4-DOF suspension roof models under blast loading.

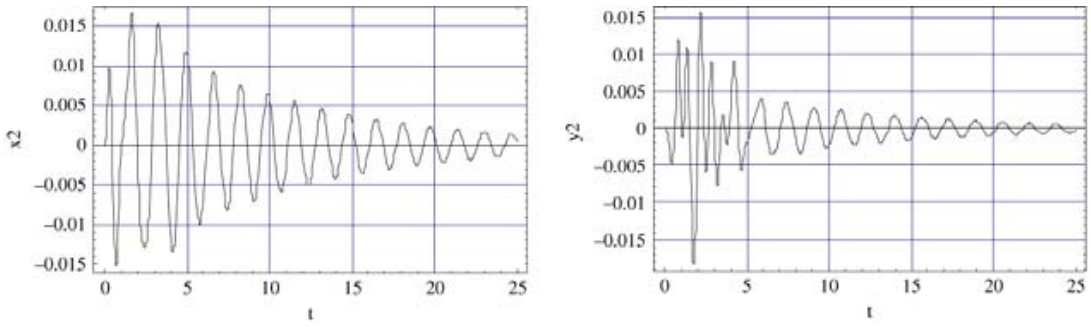

Fig. 6. Response of 3-DOF model with $\bar{k}_2 = \bar{k}_3 = 1$ under internal blast loading at the left support.

Table 1
Natural periods T of the 3-DOF model for various suspension stiffness

	$\bar{k}_2 = \bar{k}_3 = 1$	$\bar{k}_2 = \bar{k}_3 = 0.5$	$\bar{k}_2 = \bar{k}_3 = 0.1$
T_1 (s)	1.057	1.057	1.057
T_2 (s)	0.680	0.809	0.989

cases, the suspension dashpots correspond to a damping ratio $\xi = 2\%$, while the lateral support dashpots correspond to $\xi = 5\%$. Thus, in view of Eqs. (10) the values of the nondimensional dashpot coefficients are $\bar{c}_1 = \bar{c}_4 = 0.070$ and $\bar{c}_2 = \bar{c}_3 = 0.028$.

Table 1 lists the first two eigenperiods of the double suspension roof model that correspond to a horizontal and a translational mode, respectively. The fundamental period T_1 associated with the horizontal mode is not affected by the variation of the suspension stiffness, contrary to the second eigenperiod T_2 that is directly affected and dominates the vertical motion. It should be noted, at this point, that the eigenperiods listed in Table 1 (as well as in Table 2 for the triple suspension system) have been evaluated at the initial configuration of the system using a standard mode-extraction procedure for linear systems; see e.g. Graig [19]. They have been used in order to get a feel for the effect of the suspension stiffness variation on the system response. The solution of the problem is based on a nonlinear formulation and solution algorithm only.

The system is given a small initial deformation with $\theta^*_{2,0} = 0.5°$. Both the internal and external blast loads p_r are taken as 25% of the total weight of the system ($\lambda = 0.0235$). For internal blast, the arrival time is taken $t_a = 1.0$ s and the positive phase duration is $T_r = 0.5$ s, while for external blast, the raise time is $t_1 = 0.50$ s, the positive phase duration is $t_1 + t_2 = 1.5$ s and the exponential factor is $a = 1$. The loading parameters are chosen taking into account the relative criteria presented by Craig [19]. With such a selection of λ, the impact loads are just below the maximum load level that leads to excess deformation of the suspension associated with material failure of the springs.

Regarding the internal blast source position, two cases have been considered; see Fig. 5(a): (a) the blast source is located directly under node 2, and (b) the source is at equal distances from nodes 1 and 4. For external blast the source position is taken outside the system at node 1.

The system of the three nonlinear equations of motion, Eqs. (7), is thereafter treated numerically as a system of six first order ODEs via the Runge–Kutta scheme yielding a minimal error $O(h^4)$, with h being the integration step [20]. It has been found that for a step size $h < 0.005$, the numerical integration procedure is stable for all cases. In order to visualize the long-term dynamic behavior, associated with a stable point attractor response, the output data have been retrieved via Mathematica software [21], producing the representative time-series shown in Figs. 6–8 for an internal blast load near the left support. Figs. 9–11 present similar plots for internal blast at equal distances from the supports. The coordinates x_i and y_i ($i = 2, 3$) denote the horizontal and vertical response of node i, respectively, of the models subjected to blast loads. In Fig. 12, the plane portraits for node 2 are presented for the strong suspension models for internal and external blast, respectively. From these figures it can be observed that: (a) as the suspension stiffness increases the response amplitude attenuates at a slower rate, and (b) as the suspension stiffness decreases the system experiences larger amplitudes in the vertical direction. More specifically, an increase of 50%–90% of the amplitude in the horizontal direction and 200%–300% in the vertical direction is observed. Comparing internal to external blast effects, it is observed that external blast affects both the horizontal and the vertical response of the system. Specifically, the amplitude of the horizontal component increases by 50% and the amplitude of the vertical component decreases by 70%.

3.2. Triple suspension roof model

As a second case, the 4-DOF model shown in Fig. 5(b) is studied. For this model similar mass, length and stiffness properties with the 3-DOF system are selected, so that

Table 2
Natural periods T of the 4-DOF model for various suspension stiffness

	$\bar{k}_2 = 2\bar{k}_3 = \bar{k}_4 = 1$	$\bar{k}_2 = 2\bar{k}_3 = \bar{k}_4 = 0.5$	$\bar{k}_2 = 2\bar{k}_3 = \bar{k}_4 = 0.1$
T_1 (s)	1.967 (v)	1.669 (v)	1.323 (v)
T_2 (s)	1.528 (c)	1.179 (c)	1.125 (h)
T_3 (s)	0.926 (h)	0.914 (h)	0.710 (c)

Note: (h) horizontal mode, (v) vertical mode, (c) coupled vertical and rotational mode.

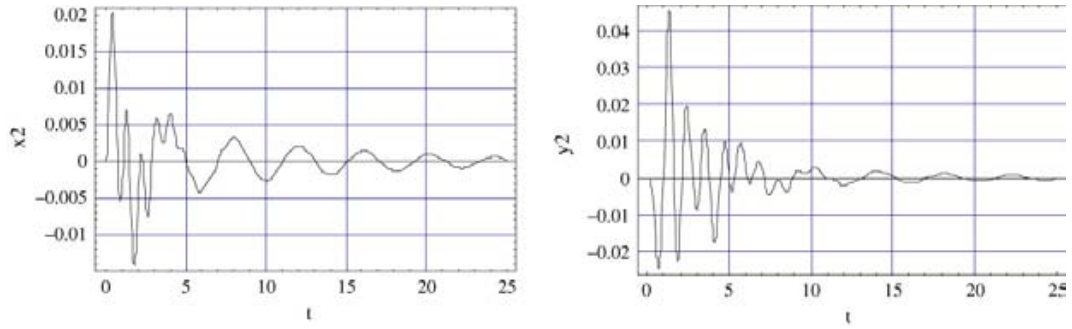

Fig. 7. Response of 3-DOF model with $\overline{k}_2 = \overline{k}_3 = 0.1$ under internal blast loading at the left support.

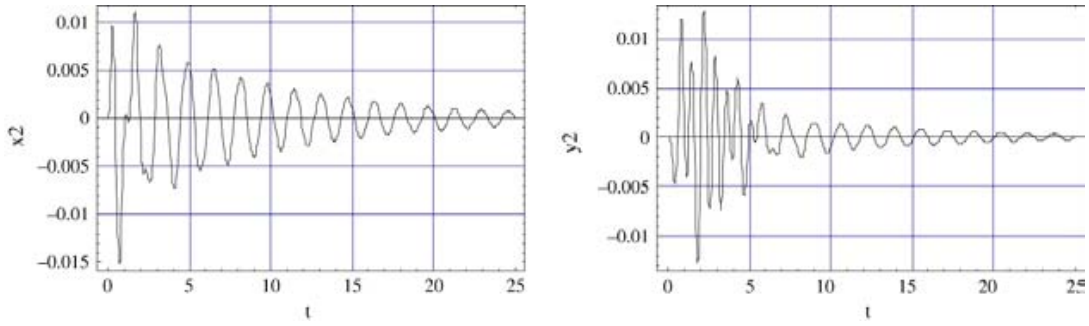

Fig. 8. Response of 3-DOF model with $\overline{k}_2 = \overline{k}_3 = 1$ under internal blast loading at equal distances from the supports.

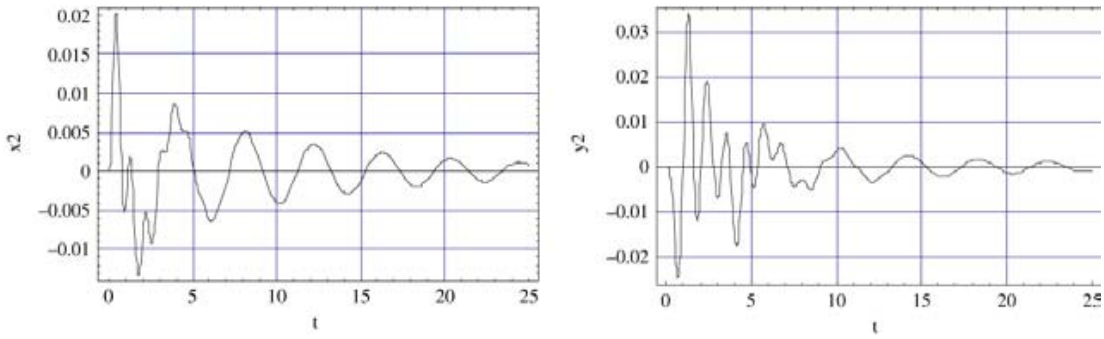

Fig. 9. Response of 3-DOF model with $\overline{k}_2 = \overline{k}_3 = 0.1$ under internal blast loading at equal distances from the supports.

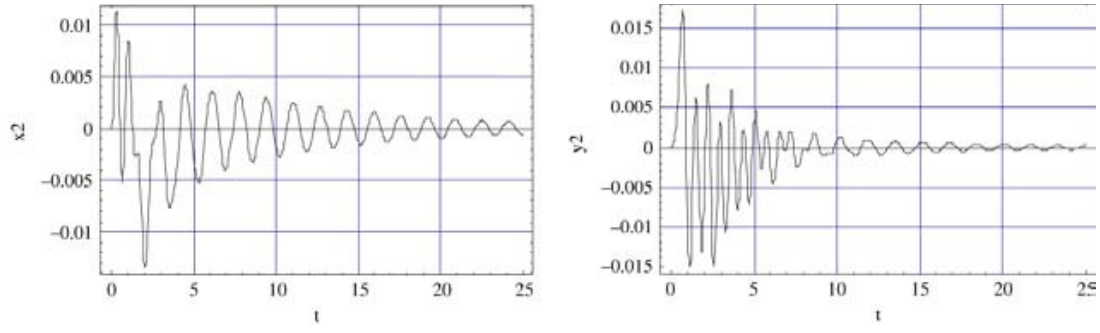

Fig. 10. Response of 3-DOF model with $\overline{k}_2 = \overline{k}_3 = 1$ under external blast loading at the left support.

$\overline{\ell}_2 = \overline{\ell}_3 = 3$, $\overline{\ell}_{4,0} = 1$, $2\overline{m}_3 = \overline{m}_4 = 0.5$, $\theta_{2,0} = -\theta_{3,0} = 30°$ and $\theta_{1,0} = -\theta_{4,0} = 45°$, in order to examine trends of the response when the suspensions of the system are increased. The suspension stiffness ($k_2 = 2k_3 = k_4$) has been varied with reference to the lateral support stiffness ($k_1 = k_5$). The following cases are considered: (i) strong suspension systems ($\overline{k}_2 = 2\overline{k}_3 = \overline{k}_4 = 1$), (ii) medium stiffness suspension system ($\overline{k}_2 = 2\overline{k}_3 = \overline{k}_4 = 0.5$), and (iii) low stiffness suspension system ($\overline{k}_2 = 2\overline{k}_3 = \overline{k}_4 = 0.1$). The suspension damping coefficients correspond to a damping ratio $\xi = 2\%$, while the lateral ones correspond to $\xi = 5\%$. As in the 3-DOF model, the 4-DOF system is also given a small initial deformation with $\theta^*_{2,0} = 0.5°$.

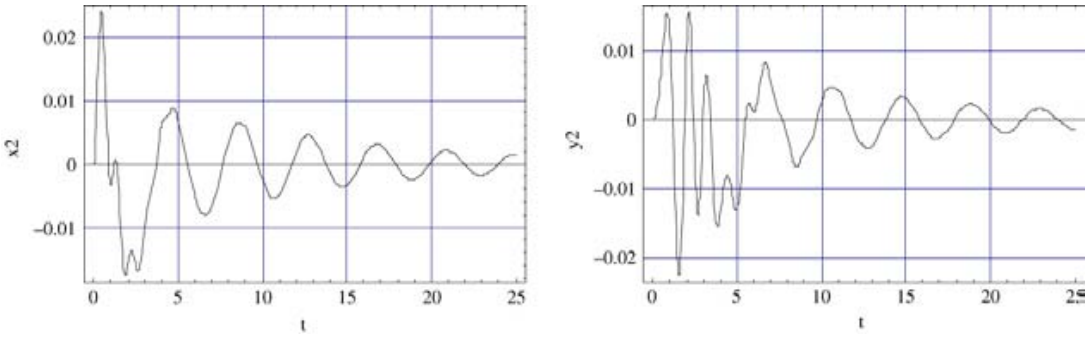

Fig. 11. Response of 3-DOF model with $\bar{k}_2 = \bar{k}_3 = 0.1$ under external blast loading at the left support.

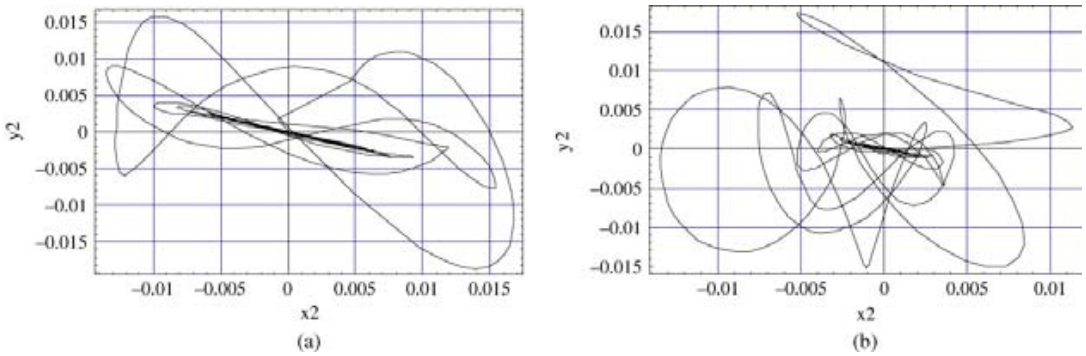

Fig. 12. Plane portraits for node 2 of 3-DOF model with $\bar{k}_2 = \bar{k}_3 = 1$ under (a) internal and (b) external blast loading at the left support.

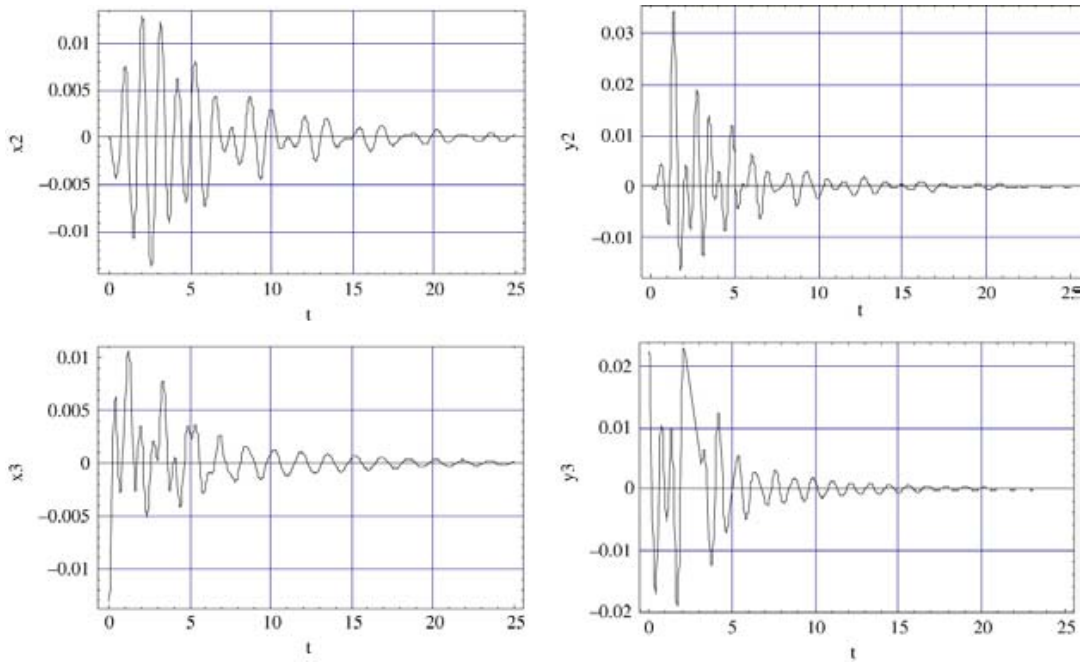

Fig. 13. Response of 4-DOF model with $\bar{k}_2 = 2\bar{k}_3 = \bar{k}_4 = 1$ under internal blast loading at the left support.

Table 2 presents the first three eigenperiods of the triple suspension roof model that correspond to horizontal translational, vertical and coupled modes, respectively. It is observed that the eigenperiod associated with the horizontal mode is slightly affected by the variation of the suspension stiffness, contrary to the other two eigenperiods that are directly affected and dominate the vertical motion. A comparison between Tables 1 and 2 shows that: (a) the triple suspension system has higher eigenperiods than the corresponding double suspension system, and (b) the suspension stiffness significantly affects the corresponding vertical and coupled rotational modes, which implies that the vertical stiffness is the primary parameter that controls the system response.

The system of four differential equations of motion Eqs. (7) is derived and then solved numerically via the Runge–Kutta scheme, and the time-series and plane portraits for three representative cases of triply suspended roofs are presented in Figs. 13–19. More specifically, the response for nodes 2

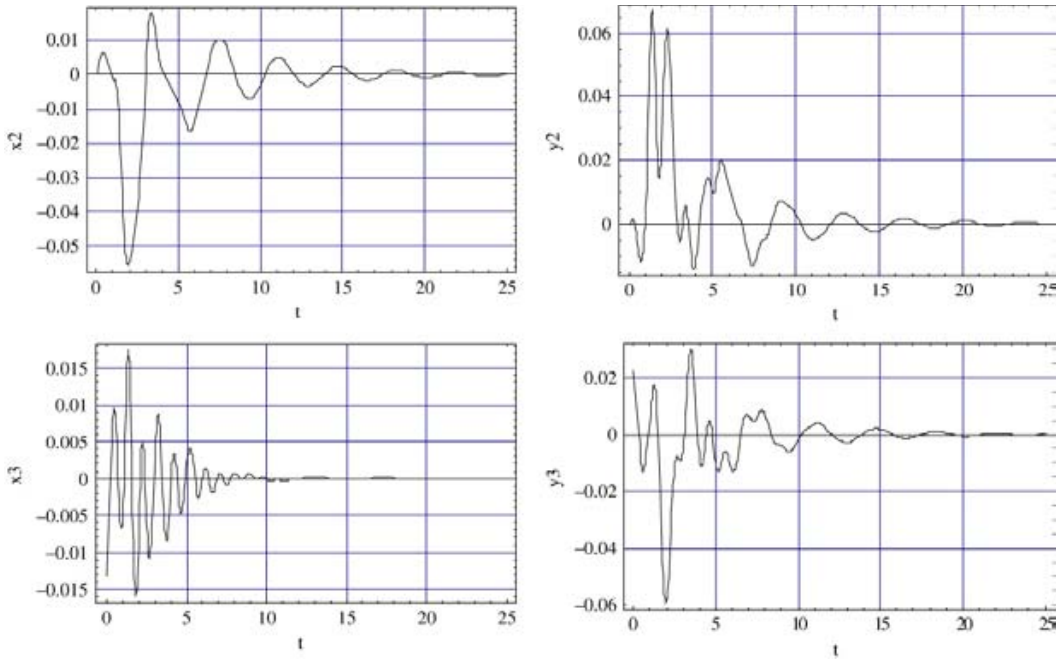

Fig. 14. Response of 4-DOF model with $\bar{k}_2 = 2\bar{k}_3 = \bar{k}_4 = 0.1$ under internal blast loading at the left support.

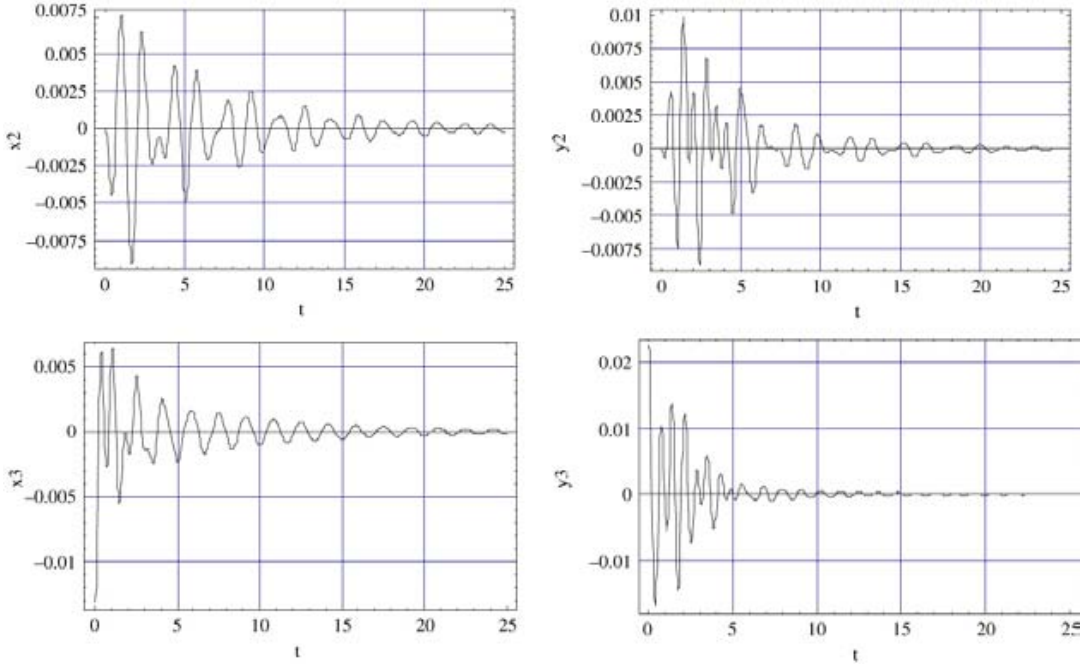

Fig. 15. Response of 4-DOF model with $\bar{k}_2 = 2\bar{k}_3 = \bar{k}_4 = 1$ under internal blast loading at equal distances from the supports.

and 3 are shown in Figs. 13 and 14 for an internal blast load directly under node 2 for various values of the suspension stiffness. Figs. 15 and 16 present the response for a blast load at equal distances from nodes 1 and 5, while Figs. 17 and 18 depict the response of the system caused by an external blast at node 1. In Fig. 19 the plane portraits for nodes 2 and 3 are presented for the strong suspension models for internal and external blast, respectively. From these figures one can arrive at the same general conclusions as for the double suspension model regarding the amplitude and duration of motion. More specifically, it is observed that as the stiffness decreases, the amplitude in the horizontal direction increases by 100%–300% and in the vertical direction by almost 200%. Comparing internal to external blast effects, it is observed that external blast affects mainly the horizontal response of the roof (amplitude increases by 70%) and has less effect on the vertical component producing smaller amplitudes (30% decrease).

Comparing the dynamic response between the double and triple suspension systems, it becomes clear that: (a) the triple suspension system experiences larger amplitudes

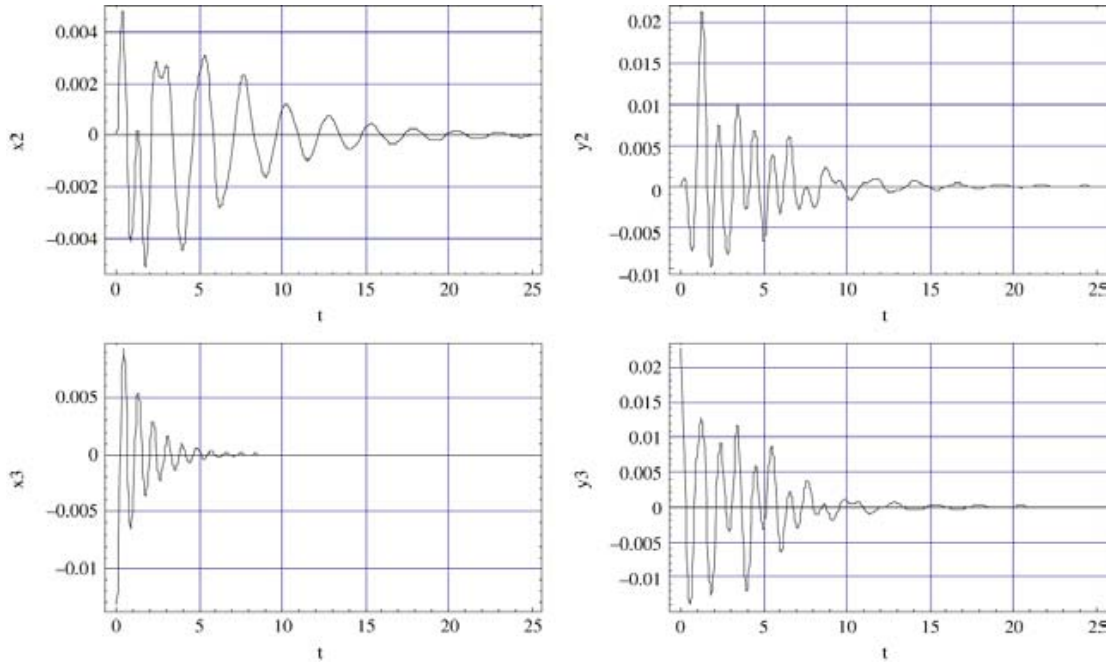

Fig. 16. Response of 4-DOF model with $\bar{k}_2 = 2\bar{k}_3 = \bar{k}_4 = 0.1$ under internal blast loading at equal distances from the supports.

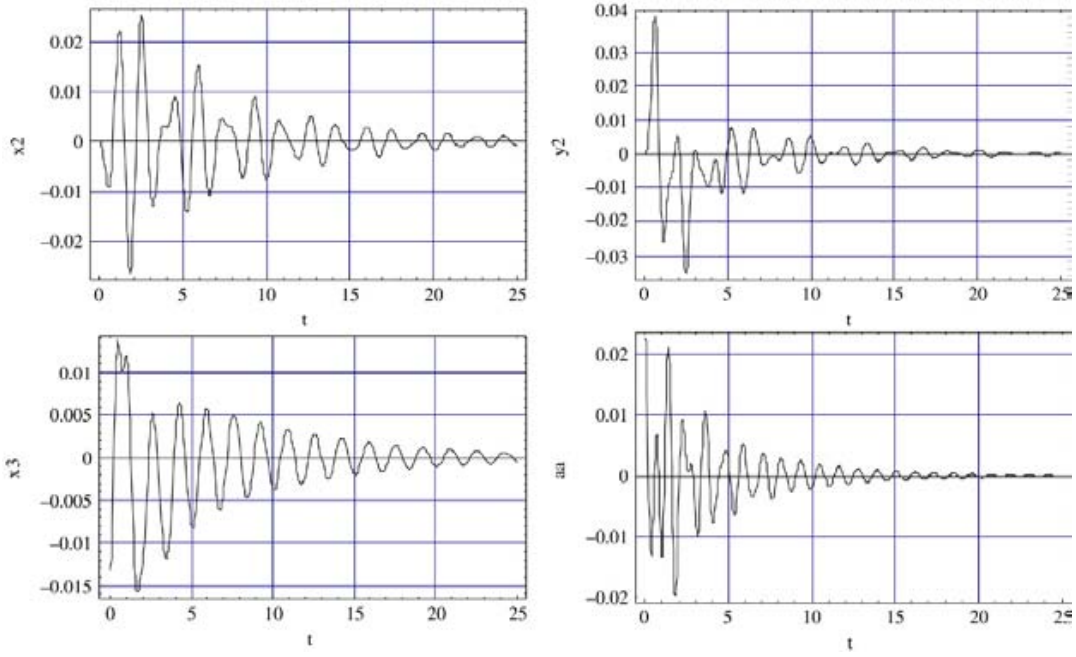

Fig. 17. Response of 4-DOF model with $\bar{k}_2 = 2\bar{k}_3 = \bar{k}_4 = 1$ under external blast loading at the left support.

in the vertical direction than the double suspension system by almost 80%–100%, (b) the external blast affects mainly the horizontal movement of the roof, and (c) the coupled vertical–rotational component, see Fig. 19, is also excited producing larger amplitudes in the vertical direction by almost 100%. The influence of geometric nonlinearity on the response of the system is illustrated through Figs. 12 and 19, where the plane-portraits of nodal displacements are shown. The highly nonlinear response of the system is due to geometric nonlinearities only, since the material is assumed linearly elastic.

4. Conclusions

A general simplified multi-DOF model to study the dynamic response of multi-suspended roof systems under internal and external blast loads is presented. The results for the 3-DOF and 4-DOF systems are qualitatively in total agreement with the ones reported in previous studies on double and multiple suspension roofs subjected to suddenly applied loads acting in the vertical direction only [13,14].

The most important conclusions in this study can be summarized as follows:

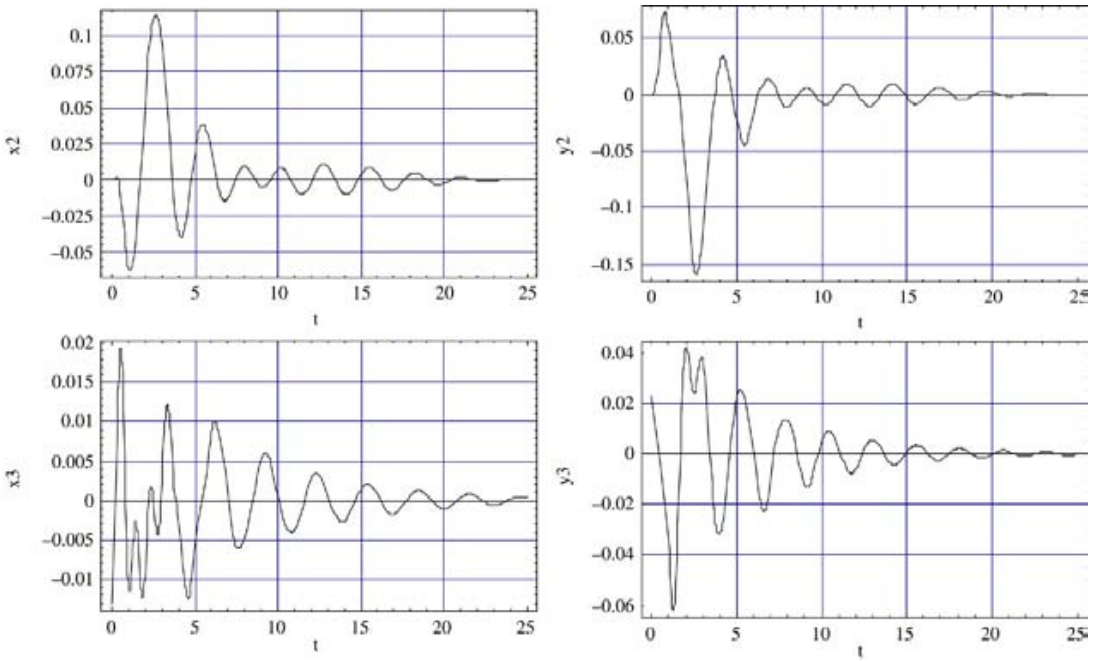

Fig. 18. Response of 4-DOF model with $\bar{k}_2 = 2\bar{k}_3 = \bar{k}_4 = 0.1$ under external blast loading at the left support.

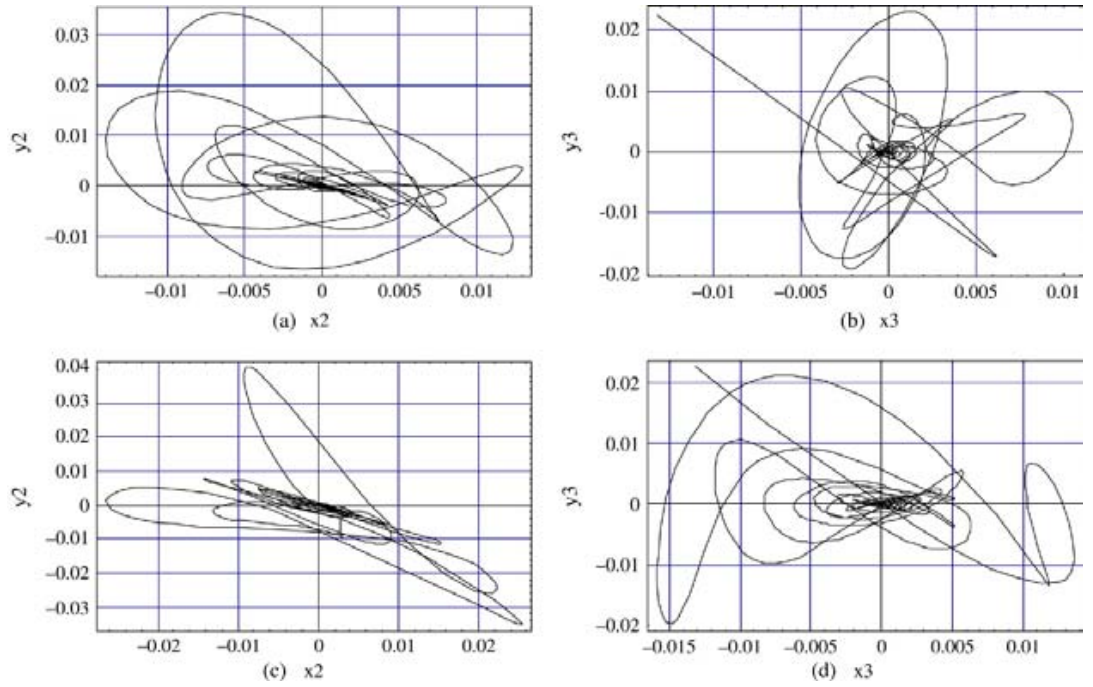

Fig. 19. Plane portraits for nodes 2 and 3 of 4-DOF model with $\bar{k}_2 = 2\bar{k}_3 = \bar{k}_4 = 1$ under (a), (b) internal and (c), (d) external blast loading at the left support.

– For all model cases dealt with, the global dynamic response of the system is observed to be stable, a primary advantage of multi-suspension roofs that is successfully captured by the proposed methodology.
– This analysis demonstrates that the stiffness of the suspension system dominates the dynamic response of the roofing system, while the effect of the stiffness of the lateral supports is proven to be less important.
– As the suspension stiffness increases the response amplitude attenuates at a slower rate for both double and triple suspension systems, while in contrast, as the suspension stiffness decreases the system experiences larger amplitudes in the vertical direction.
– Comparing the effects due to internal and external blast, it is observed that external blast influences mainly the horizontal response of the roof and has secondary effects on the vertical component, producing smaller amplitudes for double and triple suspension systems.
– In triple suspension systems, a coupled vertical–rotational mode is also excited, producing a motion with greater amplitude in the vertical direction.

– The dynamic response of stiff-suspension systems under blast loads is associated with amplitudes attenuating at a slower rate. This effect is more pronounced in double suspension systems compared to triple or more suspension systems.

It is finally concluded that the proposed multi-DOF model can serve as a tool to study the dynamic behavior of multiple suspension roofs and offers a first insight on the advantages of this popular roofing system. In addition, it can be readily employed for preliminary studies of the dynamic response and global stability of multi-suspended roof systems under blast loads.

Appendix

The three equations of motion for the 3-DOF system without damping are:

$$
\begin{aligned}
&-1 - px2\cos[\theta1[t]] - px3\cos[\theta1[t]] + l1[t]\\
&\quad - py2\sin[\theta1[t]] - py3\sin[\theta1[t]]\\
&\quad + k2\sin[\theta1[t]](-\sin[\theta10] + l1[t]\sin[\theta1[t]])\\
&\quad + k3\sin[\theta1[t]](-\sin[\theta10] - l2\sin[\theta20]\\
&\quad + l1[t]\sin[\theta1[t]] + l2\sin[\theta2[t]])\\
&\quad + (k4(-2\cos[\theta1[t]](\cos[\theta10] + l2\cos[\theta20]\\
&\quad + l30\cos[\theta30] - l2\cos[\theta2[t]] - \cos[\theta1[t]]l1[t])\\
&\quad - 2\sin[\theta1[t]](\sin[\theta10] + l2\sin[\theta20]\\
&\quad + l30\sin[\theta30] - l1[t]\sin[\theta1[t]]\\
&\quad - l2\sin[\theta2[t]]))(-l30 + \sqrt{((\cos[\theta10] + l2\cos[\theta20]}\\
&\quad + l30\cos[\theta30] - l2\cos[\theta2[t]] - \cos[\theta1[t]]l1[t])^2\\
&\quad + (\sin[\theta10] + l2\sin[\theta20] + l30\sin[\theta30]\\
&\quad - l1[t]\sin[\theta1[t]]\\
&\quad - l2\sin[\theta2[t]])^2))))/(2\sqrt{((\cos[\theta10] + l2\cos[\theta20]}\\
&\quad + l30\cos[\theta30] - l2\cos[\theta2[t]] - \cos[\theta1[t]]l1[t])^2\\
&\quad + (\sin[\theta10] + l2\sin[\theta20] + l30\sin[\theta30]\\
&\quad - l1[t]\sin[\theta1[t]] - l2\sin[\theta2[t]])^2))\\
&\quad + \frac{1}{2}(2\sin[\theta1[t]]\theta1'[t](-l1[t]\sin[\theta1[t]]\theta1'[t]\\
&\quad + \cos[\theta1[t]]l1'[t])\\
&\quad - 2\cos[\theta1[t]]\theta1'[t](\cos[\theta1[t]]l1[t]\theta1'[t]\\
&\quad + \sin[\theta1[t]]l1'[t]))\\
&\quad - \frac{1}{2}m3(-2\sin[\theta1[t]]\theta1'[t](-l1[t]\sin[\theta1[t]]\theta1'[t]\\
&\quad - l2\sin[\theta2[t]]\theta2'[t] + \cos[\theta1[t]]l1'[t])\\
&\quad + 2\cos[\theta1[t]]\theta1'[t](\cos[\theta1[t]]l1[t]\theta1'[t]\\
&\quad + l2\cos[\theta2[t]]\theta2'[t] + \sin[\theta1[t]]l1'[t]))\\
&\quad + \frac{1}{2}(-2\sin[\theta1[t]]\theta1'[t](-l1[t]\sin[\theta1[t]]\theta1'[t]\\
&\quad + \cos[\theta1[t]]l1'[t])\\
&\quad + 2\cos[\theta1[t]]\theta1'[t](\cos[\theta1[t]]l1[t]\theta1'[t]\\
&\quad + \sin[\theta1[t]]l1'[t])\\
&\quad + 2\cos[\theta1[t]](-\cos[\theta1[t]]l1[t]\theta1'[t]^2\\
&\quad - 2\sin[\theta1[t]]\theta1'[t]l1[t] - l1'[t]\sin[\theta1[t]]\theta1''[t]\\
&\quad + \cos[\theta1[t]]l1''[t])\\
&\quad + 2\sin[\theta1[t]](-l1[t]\sin[\theta1[t]]\theta1'[t]^2\\
&\quad + 2\cos[\theta1[t]]\theta1'[t]l1'[t] + \cos[\theta1[t]]l1[t]\theta1''[t]\\
&\quad + \sin[\theta1[t]]l1''[t]))\\
&\quad + \frac{1}{2}m3(-2\sin[\theta1[t]]\theta1'[t](-l1[t]\sin[\theta1[t]]\theta1'[t]\\
&\quad - l2\sin[\theta2[t]]\theta2'[t] + \cos[\theta1[t]]l1'[t])\\
&\quad + 2\cos[\theta1[t]]\theta1'[t](\cos[\theta1[t]]l1[t]\theta1'[t]\\
&\quad + l2\cos[\theta2[t]]\theta2'[t] + \sin[\theta1[t]]l1'[t])\\
&\quad + 2\cos[\theta1[t]](-\cos[\theta1[t]]l1[t]\theta1'[t]^2\\
&\quad - l2\cos[\theta2[t]]\theta2'[t]^2 - 2\sin[\theta1[t]]\theta1'[t]l1'[t]\\
&\quad - l1[t]\sin[\theta1[t]]\theta1''[t] - l2\sin[\theta2[t]]\theta2''[t]\\
&\quad + \cos[\theta1[t]]l1''[t])\\
&\quad + 2\sin[\theta1[t]](-l1[t]\sin[\theta1[t]]\theta1'[t]^2\\
&\quad - l2\sin[\theta2[t]]\theta2'[t]^2\\
&\quad + 2\cos[\theta1[t]]\theta1'[t]l1'[t] + \cos[\theta1[t]]l1[t]\theta1''[t]\\
&\quad + l2\cos[\theta2[t]]\theta2''[t]\\
&\quad + \sin[\theta1[t]]l1''[t])). \qquad \text{(A.1)}\\
&-py2\cos[\theta1[t]]l1[t] - py3\cos[\theta1[t]]l1[t]\\
&\quad + px2l1[t]\sin[\theta1[t]] + px3l1[t]\sin[\theta1[t]]\\
&\quad + k2\cos[\theta1[t]]l1[t](-\sin[\theta10] + l1[t]\sin[\theta1[t]])\\
&\quad + k3\cos[\theta1[t]]l1[t](-\sin[\theta10] - l2\sin[\theta20]\\
&\quad + l1[t]\sin[\theta1[t]] + l2\sin[\theta2[t]])\\
&\quad + (k4(2l1[t](\cos[\theta10] + l2\cos[\theta20]\\
&\quad + l30\cos[\theta30] - l2\cos[\theta2[t]]\\
&\quad - \cos[\theta1[t]]l1[t])\sin[\theta1[t]]\\
&\quad - 2\cos[\theta1[t]]l1[t](\sin[\theta10] + l2\sin[\theta20]\\
&\quad + l30\sin[\theta30] - l1[t]\sin[\theta1[t]]\\
&\quad - l2\sin[\theta2[t]]))(-l30 + \sqrt{((\cos[\theta10]}\\
&\quad + l2\cos[\theta20] + l30\cos[\theta30]\\
&\quad - l2\cos[\theta2[t]] - \cos[\theta1[t]]l1[t])^2\\
&\quad + (\sin[\theta10] + l2\sin[\theta20]\\
&\quad + l30\sin[\theta30] - l1[t]\sin[\theta1[t]]\\
&\quad - l2\sin[\theta2[t]]^2))))/(2\sqrt{((\cos[\theta10]}\\
&\quad + l2\cos[\theta20] + l30\cos[\theta30]\\
&\quad - l2\cos[\theta2[t]] - \cos[\theta1[t]]l1[t])^2\\
&\quad + (\sin[\theta10] + l2\sin[\theta20] + l30\sin[\theta30]\\
&\quad - l1[t]\sin[\theta1[t]] - l2\sin[\theta2[t]])^2))\\
&\quad + \frac{1}{2}(-2(-l1[t]\sin[\theta1[t]]\theta1'[t]\\
&\quad + \cos[\theta1[t]]l1'[t])(-\cos[\theta1[t]]l1[t])\theta1'[t]\\
&\quad - \sin[\theta1[t]]l1'[t]) - 2(-l1[t]\sin[\theta1[t]]\theta1'[t]\\
&\quad + \cos[\theta1[t]]l1'[t])(\cos[\theta1[t]]l1[t]\theta1'[t]\\
&\quad + \sin[\theta1[t]]l1'[t])\\
&\quad - \frac{1}{2}m3(2(-l1[t]\sin[\theta1[t]]\theta1'[t] - l2\sin[\theta2[t]]\theta2'[t]
\end{aligned}
$$

$$
\begin{aligned}
&+\cos[\theta1[t]]l1'[t])(-\cos[\theta1[t]]l1[t]\theta1'[t]\\
&-\sin[\theta1[t]]l1'[t])+2(-l1[t]\sin[\theta1[t]]\theta1'[t]\\
&+\cos[\theta1[t]]l1'[t])(\cos[\theta1[t]]l1[t]\theta1'[t]\\
&+l2\cos[\theta2[t]]\theta2'[t]+\sin[\theta1[t]]l1'[t]))\\
&+\frac{1}{2}(-2\cos[\theta1[t]]l1[t]\theta1'[t](-l1[t]\sin[\theta1[t]]\theta1'[t]\\
&+\cos[\theta1[t]]l1'[t])\\
&-2\sin[\theta1[t]]l1'[t](-l1[t]\sin[\theta1[t]]\theta1'[t]\\
&+\cos[\theta1[t]]l1'[t])\\
&-2l1[t]\sin[\theta1[t]]\theta1'[t](\cos[\theta1[t]]l1[t]\theta1'[t]\\
&+\sin[\theta1[t]]l1'[t])\\
&+2\cos[\theta1[t]]l1'[t](\cos[\theta1[t]]l1[t]\theta1'[t]\\
&+\sin[\theta1[t]]l1'[t])\\
&-2l1[t]\sin[\theta1[t]](-\cos[\theta1[t]]l1[t]\theta1'[t]^2\\
&-2\sin[\theta1[t]]\theta1'[t]l1'[t]\\
&-l1[t]\sin[\theta1[t]]\theta1''[t]+\cos[\theta1[t]]l1''[t])\\
&+2\cos[\theta1[t]]l1[t](-l1[t]\sin[\theta1[t]]\theta1'[t]^2\\
&+2\cos[\theta1[t]]\theta1'[t]l1'[t]+\cos[\theta1[t]]l1[t]\theta1''[t]\\
&+\sin[\theta1[t]]l1''[t]))\\
&+\frac{1}{2}m3(-2\cos[\theta1[t]]l1[t]\theta1'[t](-l1[t]\sin[\theta1[t]]\theta1'[t]\\
&-l2\sin[\theta2[t]]\theta2'[t]+\cos[\theta1[t]]l1'[t])\\
&-2\sin[\theta1[t]]l1'[t](-l1[t]\sin[\theta1[t]]\theta1'[t]\\
&-l2\sin[\theta2[t]]\theta2'[t]+\cos[\theta1[t]]l1'[t])\\
&-2l1[t]\sin[\theta1[t]]\theta1'[t](\cos[\theta1[t]]l1[t]\theta1'[t]\\
&+l2\cos[\theta2[t]]\theta2'[t]+\sin[\theta1[t]]l1'[t])\\
&+2\cos[\theta1[t]]l1'[t](\cos[\theta1[t]]l1[t]\theta1'[t]\\
&+l2\cos[\theta2[t]]\theta2'[t]+\sin[\theta1[t]]l1'[t])\\
&-2l1[t]\sin[\theta1[t]](-\cos[\theta1[t]]l1[t]\theta1'[t]^2\\
&-l2\cos[\theta2[t]]\theta2'[t]^2-2\sin[\theta1[t]]\theta1'[t]l1'[t]\\
&-l1[t]\sin[\theta1[t]]\theta1''[t]\\
&-l2\sin[\theta2[t]]\theta2''[t]+\cos[\theta1[t]]l1''[t])\\
&+2\cos[\theta1[t]]l1[t](-l1[t]\sin[\theta1[t]]\theta1'[t]^2\\
&-l2\sin[\theta2[t]]\theta2'[t]^2+2\cos[\theta1[t]]\theta1'[t]l1'[t]\\
&+\cos[\theta1[t]]l1[t]\theta1''[t]\\
&+l2\cos[\theta2[t]]\theta2''[t]+\sin[\theta1[t]]l1''[t]))
\end{aligned}
\tag{A.2}
$$

$$
\begin{aligned}
&-l2py3\cos[\theta2[t]]+l2px3\sin[\theta2[t]]\\
&+k3l2\cos[\theta2[t]](-\sin[\theta10]-l2\sin[\theta20]\\
&+l1[t]\sin[\theta1[t]]+l2\sin[\theta2[t]])\\
&+(k4(2l2(\cos[\theta10]+l2\cos[\theta20]\\
&+l30\cos[\theta30]-l2\cos[\theta2[t]]\\
&-\cos[\theta1[t]]l1[t])\sin[\theta2[t]]\\
&-2l2\cos[\theta2[t]](\sin[\theta10]+l2\sin[\theta20]\\
&+l30\sin[\theta30]-l1[t]\sin[\theta1[t]]\\
&-l2\sin[\theta2[t]]))(-l30+\sqrt{((\cos[\theta10]+l2\cos[\theta20]\\
&+l30\cos[\theta30]-l2\cos[\theta2[t]]-\cos[\theta1[t]]l1[t])^2\\
&+(\sin[\theta10]+l2\sin[\theta20]+l30\sin[\theta30]\\
&-l1[t]\sin[\theta1[t]]-l2\sin[\theta2[t]])^2)))/(2\sqrt{((\cos[\theta10]\\
&+l2\cos[\theta20]+l30\cos[\theta30]-l2\cos[\theta2[t]]\\
&-\cos[\theta1[t]]l1[t])^2+(\sin[\theta10]+l2\sin[\theta20]\\
&+l30\sin[\theta30]-l1[t]\sin[\theta1[t]]-l2\sin[\theta2[t]])^2}))\\
&-\frac{1}{2}m3(-2l2\cos[\theta2[t]]\theta2'[t](-l1[t]\sin[\theta1[t]]\theta1'[t]\\
&-l2\sin[\theta2[t]]\theta2'[t]+\cos[\theta1[t]]l1'[t])\\
&-2l2\sin[\theta2[t]]\theta2'[t](\cos[\theta1[t]]l1[t]\theta1'[t]\\
&-l2\cos[\theta2[t]]\theta2'[t]+\sin[\theta1[t]]l1'[t]))\\
&+\frac{1}{2}m3(-2l2\cos[\theta2[t]]\theta2'[t](-l1[t]\sin[\theta1[t]]\theta1'[t]\\
&-l2\sin[\theta2[t]]\theta2'[t]+\cos[\theta1[t]]l1'[t])\\
&-2l2\sin[\theta2[t]]\theta2'[t](\cos[\theta1[t]]l1[t]\theta1'[t]\\
&+l2\cos[\theta2[t]]\theta2'[t]+\sin[\theta1[t]]l1'[t])\\
&-2l2\sin[\theta2[t]](-\cos[\theta1[t]]l1[t]\theta1'[t]^2\\
&-l2\cos[\theta2[t]]\theta2'[t]^2-2\sin[\theta1[t]]\theta1'[t]l1'[t]\\
&-l1[t]\sin[\theta1[t]]\theta1''[t]-l2\sin[\theta2[t]]\theta2''[t]\\
&+\cos[\theta1[t]]l1''[t])\\
&+2l2\cos[\theta2[t]](-l1[t]\sin[\theta1[t]]\theta1'[t]^2\\
&-l2\sin[\theta2[t]]\theta2'[t]^2+2\cos[\theta1[t]]\theta1'[t]l1'[t]\\
&+\cos[\theta1[t]]l1[t]\theta1''[t]+l2\cos[\theta2[t]]\theta2''[t]\\
&+\sin[\theta1[t]]l1''[t]))
\end{aligned}
\tag{A.3}
$$

References

[1] Otto F. Das hangende Dach. Berlin: Bauwelt Verlag; 1954.

[2] Rabinovich L. Hangerdacher. Wiesbaden: Bauverlag Gmbh; 1962.

[3] Nervi PL. New structures. London: The Architectural Press; 1963.

[4] Kultermann U, Kenzo T. Works and projects. Barcelona: G.Gilli; 1989.

[5] Saafan AS. Theoretical analysis of suspension roofs. J. Struct. Div. ASCE 1970;96(2):393–405.

[6] Scalzi JB. Cable-suspended roof construction State-of-the-Art. J. Struct. Div. ASCE 1971;97(6):1715–61.

[7] Kunieda H. Parametric resonance of suspension roofs in wind. J. Eng. Mech. Div. 1976;102(1):59–75.

[8] Morris NF. Analysis of cable-stiffened space structures. J. Struct. Div. ASCE 1976;102(3):501–13.

[9] Spyrakos CC. Finite element modeling in engineering practice. Morgantown, WV: WVU Press; 1995.

[10] Spyrakos CC, Raftoyiannis IG. Linear and nonlinear finite element analysis in engineering practice. Pittsburgh (PA): Algor Publishing Div.; 1997.

[11] Szabo J, Kollar L. Structural design of cable-suspended roofs. Chichester (UK): Ellis Norwood; 1984.

[12] Buchholdt R. Introduction to cable roof structures. 2nd ed. London: Thomas Telford; 1998.

[13] Sophianopoulos DS, Michaltsos GT. Nonlinear stability of a simplified model for the simulation of double suspension roofs. Engineering Structures 2001;23:705–14.

[14] Raftoyiannis IG, Michaltsos GT. Nonlinear dynamic stability of multi-suspended roof systems, In: CD-ROM Proceedings, XXI Int. Congress of Theoretical & Applied Mechanics. 2004.

[15] Baker WE, Cox PA, Westine PS, Kulesz JJ, Strehlow RA. Explosion hazards and evaluation. UK: Elsevier; 1983.

[16] Bangash MYH. Impact and explosion: analysis & design. Boca Raton,

Florida: CRC Press Inc.; 1993.
[17] Mays GC, Smith PD. Blast effects on buildings. London: Thomas Telford; 1995.
[18] Wagner R. Cable and membrane structures. Berlin: Ernst & Sohn; 2002.
[19] Craig RR. Structural dynamics. New York: John Willey & Sons; 1981.
[20] Davis PJ, Rabinowitz P. Methods of numerical integration. 2nd ed. New York: Academic Press; 1975.
[21] Wolfram S. Mathematica. 4th ed. UK: Cambridge University Press; 1999.